CHEMISTRY
A European Journal

A Journal of
ChemPubSoc Europe

Accepted Article

Title: Gallium Modified HUSY Zeolite as an Effective Cosupport for NiMo Hydrodesulfurization Catalyst and the Catalyst's High Isomerization Selectivity

Authors: Wenwu Zhou, Yasong Zhou, Qiang Wei, Lin Du, Sijia Ding, Shujiao Jiang, Yanan Zhang, and Qing Zhang

To be cited as: *Chem. Eur. J.* 10.1002/chem.201701307

Link to VoR: http://dx.doi.org/10.1002/chem.201701307

Supported by
ACES

WILEY-VCH

10.1002/chem.201701307

Manuscript

Gallium Modified HUSY Zeolite as an Effective Cosupport for NiMo Hydrodesulfurization Catalyst and the Catalyst's High Isomerization Selectivity

Wenwu Zhou, Yasong Zhou*, Qiang Wei, Lin Du, Sijia Ding, Shujiao Jiang, Yanan Zhang and Qing Zhang

State Key Laboratory of Heavy Oil Processing, China University of Petroleum, Beijing 102249, PR China

***Corresponding Author**

Phone: 0086 010 89733501.

E-mail: zhouyasong2011@163.com.

10.1002/chem.201701307

Abstract:

The effects of metal-modified acidic cosupports on the HDS activity and isomerization selectivity of highly refractory organosulfur compounds such as 4,6-dimethyldibenzothiophene have been investigated. Y crystals with high Si/Al ratios and small crystallite sizes were successfully synthesized by a new hydrothermal synthesis approach. The synthesized Y crystals were ion-exchanged and stabilized. The prepared samples were then modified with different gallium contents using a impregnation method to adjust their acidity properties, and these modified samples were used as cosupports for NiMo sulfide hydrodesulfurization (HDS) catalysts. The catalyst containing 10 wt.% Y zeolite modified by 2 wt.% gallium (NiMo/2GaY-ASA-A) exhibited the highest HDS activity, with 4,6-dimethyldibenzothiophene (4,6-DMDBT) conversion nearly double the rate of the catalyst without zeolite at 563 K, 4.0 MPa and LHSV of 40 h^{-1}. NiMo/2GaY-ASA-A also exhibited superior isomerization ability, with 3,4'-DMBP, 4,4'DMBP and 3,6-DMDBT as the main products, indicating that the isomerization pathway was the main reaction route over NiMo/2GaY-ASA-A. The superior catalytic performance is related to the synergistic effect of the proper amount of medium and strong Brønsted acid sites. The compounds 3,6-DMDBT and 3,7-DMDBT (isomers of 4,6-DMDBT) and 3,4,6-TMDBT and tetra-methyl-DBT (transmethyl products) were detected simultaneously in the HDS product of 4,6-DMDBT for the first time over NiMo/ GaY-ASA-A catalysts. Finally, a new reaction network over NiMo/2GaY-ASA-A was proposed.

KEYWORDS: gallium-modified HUSY, 4,6-DMDBT hydrodesulfurization, isomerization, transmethylation, selectivity

1. Introduction

SO_2 emitted by the combustion of organosulfur compounds in diesels has a significant negative impact on the atmosphere, the environment and human health. The reduction of the sulfur content in diesel fuels has received much attention in recent years due to stringent environmental legislation worldwide. To meet this requirement, hydrodesulfurization (HDS) has high potential for the removal of sulfur atoms from diesel fuels[1,2]. The greatest challenge in ultra-deep (with S content below 10 ppm) HDS is the removal of highly refractory organosulfur compounds such as 4,6-dimethyldibenzothiophene (4,6-DMDBT) from diesel fuels because the steric hindrance of the methyl groups at the 4 and 6 positions strongly restricts desulfurization[2~5]. The catalysts commonly employed in the petrochemical industry to remove sulfur atoms from transportation fuels are cobalt- or nickel-promoted MoS_2 or WS_2 supported on γ-alumina[3~6]. Highly refractory sulfur-containing compounds such as 4,6-DMDBT undergo HDS by direct desulfurization (DDS) and hydrogenation desulfurization (HYD) over conventional catalysts[2,4,7~10]: DDS produces 3,3'-dimethylbiphenyl (3,3'-DMBP) as the desulfurized product, and HYD produces tetrahydro- and hexahydro- 4,6-DMDBT as intermediates, which can be further desulfurized to yield 3,3'-dimethylcyclohexylbenzenes (3,3'-DMCHB) and 3,3'-dimethylbicyclohexyls (3,3'-DMBCH). Due to the hindrance caused by the two methyl groups at the 4 and 6 positions, which strongly prevent the adsorption of the sulfur atom at the active sites of the catalysts through sigma-adsorption, sulfur removal from 4,6-DMDBT mainly proceeds through the HYD pathway[4,11,12,13]. Thus, catalysts must possess both high hydrogenation activity to achieve the hydrogenation of aromatic rings and high hydrogenolysis activity to achieve the removal of sulfur atoms[14-16]. However, these commercial catalysts do not eliminate the hindrance caused by the methyl groups at the 4 and 6 positions, and thus it remains difficult to remove sulfur atoms from

4,6-DMDBT molecules. To overcome these drawbacks, catalysts should posess both high hydrogenation activity to promote the saturation of aromatic rings and high methyl migration activity to promote the isomerization of substituted DBTs. And acidic supports with high methyl migration activity, especially zeolites, are widely used as cosupports for HDS catalysts[4,17,18]. Zhang et al.[19] observed that cyclohexenyl benzene, one of the desulfurized products of dibenzothiophene (DBT), was isomerized to dimethyldecalin over an acidic Beta-KIT-6-supported NiMo catalyst. Moreover, many nanocrystalline zeolites[20-24], such as Y, ZSM-5 and beta, show higher catalytic activities and lower deactivation rates than conventional ones. Among all investigated materials, Y zeolites are the most suitable acidic cosupports for high refractory sulfur-containing compounds such as 4,6-DMDBT because their microporosity is comparable to the size of 4,6-DMDBT molecules. HDS catalysts containing Y zeolites as a cosupport exhibit relatively high isomerization ability, enabling the highly efficient HDS of highly refractory organosulfur compounds such as 4,6-DMDBT in inferior diesel fuels[4,10,11]. However, the acid strength, acid density, acid type and even textural properties of Y zeolites cannot satisfy the demands of 4,6-DMDBT HDS. To improve the catalytic performance of Y zeolites, the modification of Y zeolites using different metals is of great importance to adjust the acidic properties and textural properties of Y zeolite[25,26]. This has a beneficial effect for either the adsorption process or the reaction process in producing ultra clean diesels. Dapsens et al.[27] modified Y zeolite with gallium and investigated the selective conversion of bio-based dihydroxyacetone. They concluded that the post-synthetic alkaline-assisted galliation of FAU-type zeolites generated outstanding acid catalysts. In addition, gallium-modified zeolites were highly efficient for the isomerization of dihydroxyacetone. Moreover, E. Altamirano et al.[28,29]

employed gallium as an additive to investigate the effect of gallium over NiMo/Al_2O_3 catalyst and NiW/Al_2O_3 catalyst. They concluded that small amount of gallium can promote the catalytic activity of the corresponding catalysts for 4,6-DMDBT HDS due to the fact that tetrahedral coordinated gallium species over Al_2O_3 supports enhanced the sulfidability of Ni and Mo(W) species and caused more Ni species participating in the decoration of NiMoS phase. Thus, we modified HUSY zeolites with gallium as a co-support for a hydrotreating catalyst. After HUSY zeolites are modified by gallium, some of the Si-O(H)-Al bonds can be substituted by Si-O(H)-Ga bonds[30] because the Ga-O(H)-Si sites are more covalent than the Al-O(H)-Si sites. Moreover, the average electronegativity value of 1.59 for Ga is lower than the value for Al (1.714)[31], implying a lower acid strength of Brønsted protons for Ga-substituted zeolites. Previous studies have indicated that gallium-containing zeolites can effectively decrease the production of lower C1-C5 hydrocarbons and polyaromatic products in many petrochemical processes[32,33]. This decrease occurs mainly because gallium species deposited on zeolites significantly improve the hydrogenation activity of zeolites and lower the acid strength of the modified zeolites to avoid the over-cracking of the hydrogenated hydrocarbons. Since the mechanistic studies of alkanes aromatizing into aromatics indicates that gallium species deposited on zeolites have a significant effect on the adsorption and activation of alkanes to produce activated C^+ intermediates, we also hypothesized that gallium-modified zeolites exhibit extraordinary activity for the isomerization of hydrocarbons compared to conventional ones.

To test these hypotheses, we synthesized a nanocrystallite NaY zeolite with a high SiO_2/Al_2O_3 ratio and high crystallinity. The synthesized zeolites were hydrothermally treated and then modified using different contents of gallium, and the corresponding Ni-Mo HDS catalysts were

synthesized. The effects of gallium modification on the acidity and textural properties of HUSY zeolites were investigated, and the effects of gallium modification on the acidity, textural properties and active-phase morphology were also investigated for the first time. Moreover, the effects of medium and strong Brønsted acidity on catalytic performance and isomerization selectivity were investigated. The highest activity for the HDS of 4,6-DMDBT was observed over NiMo/2GaY-ASA-A, which exhibited the highest isomerization selectivity. All the catalysts' supports are composed of 10 wt.% zeolite, 20 wt.% ASA and 70 wt.% Al2O3, the catalysts are composed of 5 wt.% NiO, 15 wt.% MoO3 and 80 wt.% support. Finally, we proposed a reaction network involving the isomerization and transmethylation of 4,6-DMDBT and related intermediate products for the HDS of 4,6-DMDBT over NiMo/GaHUSY-ASA-γ-Al_2O_3 catalyst. To clarify the effect of gallium modification, the HDS reaction of 4,6-DMDBT was also studied over a gallium-free zeolite-containing catalyst.

2. Experimental Section

2.1 Catalyst preparation

All NaY zeolites were synthesized via a new two-stage variable temperature crystallization program. In a typical synthesis, 2.0 g of sodium hydroxide, 77 g of sodium silicate (28 wt.% SiO_2, 9.1 wt.% Na_2O, and 62.9 wt.% H_2O), 3.25 g of sodium aluminate, 3.5 g of aluminum sulfate, 20 g of deionized water and 10 g of synthesized structural directing agent were mixed under vigorous agitation, and the precursor gel composition was 7.5:1:16:240 $Na_2O/Al_2O_3/SiO_2/H_2O$. The mixed gel was then aged at 315 K for 18 h and then pre-crystallized at 335 K in a Teflon autoclave. Finally, the pre-crystallized system was hydrothermally crystallized at 368 K for another 24 h, washed with deionized water, and calcined at 823 K for 5 h. The synthesized NaY zeolites were

ion-exchanged with 1.0 M NH_4NO_3 aqueous solution 3 times at 363 K for 4 h and then calcined at 823 K for 5 h in a muffle furnace to obtain HY zeolites. The obtained HY zeolites were stabilized by treating with citric acid (weight ratio of citric acid to HY zeolite = 1:12, Beijing Modern Oriental Fine Chemical Co. Ltd., ≥99.8 %), and the product was denoted ultra-stable HY (HUSY) zeolite. Gallium-modified HUSY zeolites with different Ga contents were prepared by incipient wetness impregnation with a calculated aqueous solution of gallium nitrate (Aladdin, ≥99.9 %). The obtained samples were dried at 393 K for at least 6 h after the evaporation of the solvent at room temperature overnight, then calcined at 823 K for 5 h in a muffle furnace. The modified zeolites containing 1 % Ga_2O_3, 2 % Ga_2O_3 and 3 % Ga_2O_3 were denoted 1GaHUSY, 2GaHUSY and 3GaHUSY, respectively. Amorphous silica-alumina (ASA) was prepared as described elsewhere in the literature [24], and the pseudo-boehmite was purchased from Shangdong Aluminium Factory (Zibo, Shangdong). The gallium-modified HUSY, prepared ASA and purchased pseudo-boehmite were mechanically mixed at a mass ratio of 1:2:7, extruded to form a four leaf clover-cylindrical shape and crushed into 20 to 40 mesh. Ni-Mo catalysts were prepared via an incipient wetness co-impregnation method with an aqueous solution of appropriate amounts of nickel nitrate hexahydrate and ammonium heptamolybdate tetrahydrate, then dried at 393 K for 6 h after vaporization at room temperature overnight and calcined at 823 K for 5 h. The catalysts were designated NiMo/Y-ASA-A, NiMo/1GaY-ASA-A, NiMo/2GaY-ASA-A and NiMo/3GaY-ASA-A, where the number represents the mass content of gallium in the HUSY zeolites. For all the synthesized catalysts, the total concentration of NiO in the catalysts was 5 wt.%, and the total MoO_3 concentration was 15 wt.% in the catalysts. A reference catalyst, NiMo/ASA-A was also prepared by the same process except that the support consisted of 30 wt.%

ASA and 70 wt.% Al_2O_3.

2.2 Material characterization

The powder X-ray diffraction (XRD) patterns of all synthesized and modified zeolites were recorded on a PANalytical advance powder diffractometer with Cu Kα radiation (40 kV, 40 mA) in the 2θ interval of 5~35°. The crystallite size of the synthesized zeolite was observed by field emission scanning electron microscopy (SEM) on a Quanta 200F instrument, and the crystallite size was statistically analyzed by counting at least 500 crystals. The Si, Al and Ga contents in the synthesized zeolites were determined by inductively coupled plasma atomic emission spectroscopy (ICP-AES) on a PE OPTIMA 5300DV instrument. Nitrogen adsorption-desorption measurements were performed at 77 K using a Micromeritics ASAP 2010 analyzer on degassed samples (10^{-1} mbar, 573 K, 4 h). The surface area of the examined samples was determined using the Brunauer-Emmett-Teller (BET) equation, and the pore volume and pore diameter were obtained using the Barrett-Joyner-Halenda (BJH) method with the N_2 adsorption isotherm. NH_3 temperature-programmed desorption (NH_3-TPD) of the obtained materials was performed on a Chembet 3000 chemical adsorption instrument. All measured materials were pretreated at 823 K for 60 min in a mixture of Ar and air flow (v:v=3:1) and then cooled to 393 K and allowed to adsorb NH_3 for 30 min. Afterwards, the physically adsorbed NH_3 was removed in an Ar flow for 90 min. The furnace temperature was then programmed to increase at a rate of 10 K/min from 393 K to 1023 K in 65 min. The amount of desorbed ammonia was detected by continuous effluent gas monitoring equipped with a thermal conductivity detector (TCD). To assess the acidity of zeolites and catalysts, pyridine-adsorbed Fourier transform infrared measurements (Py-FTIR) were conducted on a Magna 560 FT-IR analyzer. The samples were dehydrated at 673 K for 3 h under a

vacuum of 10^{-2} Pa. Then, pure pyridine vapor was fed to the measured sample at room temperature for 30 min, obtaining the saturated adsorption of py-FTIR spectra. The adsorbed pyridine was then evacuated at 473 K, 553 K and 623 K for 60 min in turn, to obtain the desorption of py-FTIR spectra at 473 K, 553 K and 623 K, respectively. H_2 temperature-programmed reduction (H_2-TPR) patterns of all the investigated catalysts were recorded on a TP-5000 multifunction adsorption instrument. Before the TPR measurement, the catalyst was pretreated at 673 K for 60 min in air flow. Then, the reducing gas (H_2/Ar = 1:19, v:v) was fed to the tested sample at a flow rate of 30 mL/min, and simultaneously, the furnace temperature was programmed to increase at a rate of 10 K/min from 393 K to 1273 K. The HRTEM images of all sulfide catalysts were taken on a Philips Tecnai G2 F20 instrument with an operating electron voltage of 200 kV. At least 500 slabs taken from different parts of each catalyst were counted to determine the size distribution of molybdenum sulfide crystallites. We calculated the average length and stack number of MoS_2 slabs using equations reported elsewhere as follows[34,35]:

Average slab length: $$\bar{L} = \sum_{i=1}^{n} n_i l_i \Big/ \sum_{i=1}^{n} n_i \quad (1)$$

Average stack number: $$\bar{N} = \sum_{i=1}^{n} n_i N_i \Big/ \sum_{i=1}^{n} n_i \quad (2)$$

where l_i is the length of the slab, n_i is the number of slabs with length l_i, and N_i is the number of layers in slab i. The MoS_2 dispersion f_{Mo} was also calculated using the following equation reported in the literature[4,36]:

$$f_{Mo} = \frac{Mo_{edge}}{Mo_{total}} = \frac{\sum_{i=1}^{t} 6(n_i - 1)}{\sum_{i=1}^{t} (3n_i^2 - 3n_i + 1)} \quad (3)$$

where Mo_{edge} is the number of Mo atoms located on the edges of NiMoS slabs, Mo_{total} is the total number of Mo atoms, n_i is the number of Mo atoms along one edge of a MoS_2 slab

determined from its length ($L = 3.2(2n_i - 1)$Å), and t is the total number of slabs determined by at least 500 MoS_2 slabs taken from HRTEM images of different catalysts. The positions of the introduced gallium species were measured by X-ray photoelectron spectroscopy (XPS) on a VG ESCA Lab 250 spectrometer using Al Kα radiation as the excitation light source. Prior to the test, the C 1s peak with a binding energy of 284.6 eV and the Al 2p peak with a binding energy of 74.6 eV were used to calibrate the binding energy scale.

2.3 Catalyst evaluation

HDS reactions of 4,6-DMDBT were performed on a fixed-bed reactor (8 mm inner diameter and 500 mm in length) loaded with 2 g of catalyst with a particle size of 0.59–0.84 mm in diameter diluted by 5 mL of quartz sand. Before the assessment, the catalyst was presulfided using a solution of 6.0 mL CS_2 dissolved in 500 mL of cyclohexane at 593 K and 4 MPa for 6 h in a H_2 flow of 1200 mL min^{-1} with a liquid hourly space velocity (LHSV) of 10 h^{-1}. After that, the reactor temperature was decreased to 563 K, and a mixture of 0.5 wt.% of 4,6-DMDBT dissolved in cyclohexane was pumped to the reactor using an SZB-2 double-piston pump. The 4,6-DMDBT HDS evaluations were conducted at temperatures of 558 K to 573 K, a total pressure of 4.0 MPa, a liquid hourly space velocity (LHSV) of 10.0 h^{-1} to 150 h^{-1}, and a hydrogen/oil ratio of 120 (v/v). The liquid reaction products were carefully collected after a full stabilization period of 12 h. Then, the collected products were immediately analyzed off-line on an Agilent 4890D gas chromatograph equipped with a 60-m capillary Rtx-1 column (0.25 mm, RESREK) with a N_2 pressure of 0.3 MPa and flow velocity of 30 mL min^{-1} as the column temperature increased from 323 K to 593 K with a heat rate of 15 K min^{-1} after staying at 323 K for 1 min. To further identify each of the compounds in the liquid products, a Finnigan Trace GC–MS consisting of a Trace

Ultral gas chromatograph (60 m - 0.25 mm - 0.5 μm) capillary column and an MS detector HP 5973 was used to analyze the collected products.

The global rate constant (k_{HDS}) of 4,6-DMDBT HDS reactions were calculated by employing the pseudo-first order reaction according to the following two equations[4]:

$$k_{HDS} = -{}^{F}/_{m} \ln(1-x) \quad (4)$$

where k_{HDS} stands for the reaction rate constant for the pseudo-first order reaction in mol g^{-1} h^{-1}, which is calculated by changing the reactant feeding rate, F is the reactant feed to the reactor in mol h^{-1}, m is the mass of the loaded catalyst in grams, and x is the total conversion of 4,6-DMDBT.

The activation energies of 4,6-DMDBT HDS reactions over all the mentioned catalysts at 563 K were calculated by employing a pseudo-first order reaction according to equation 5[30,33] by fixing the LHSV at 40 h^{-1} and varied the reaction temperature in the range of 558 K to 573 K at an interval of 5 K:

$$\text{Ea} = {}^{RTln(\frac{x1}{x2})}/_{(T1-T2)} \quad (5)$$

where Ea is the activation energy in kJ mol^{-1}, $x1$ is the 4,6-DMDBT conversion at higher reaction temperature ($T1$), $x2$ is the 4,6-DMDBT conversion at lower reaction temperature ($T2$).

3. Results

3.1 Textural properties

The XRD patterns of the synthesized NaY, HY, USY and HUSY zeolites and of HUSY modified with different contents of gallium are shown in S1 and Fig. 1. All materials present the typical diffraction features of FAU zeolites, and no diffraction peaks related to gallium species were observed, indicating the formation of FAU zeolite cells and an intact FAU zeolite structure

after the modification process[5]. However, the lower intensities of the diffraction peaks imply lower crystallinity after the ion-exchange process, stabilization process and modification process. The crystallinity and framework SiO_2/Al_2O_3 molar ratio of the synthesized zeolites were obtained and are listed in Table 1. The framework SiO_2/Al_2O_3 molar ratio of the synthesized NaY zeolite was 5.8. After ion-exchange and citric acid treatment of the NaY zeolite, the framework SiO_2/Al_2O_3 molar ratio increased to approximately 12.5 and 14.9 for the HY and USY zeolites, respectively. The SiO_2/Al_2O_3 molar ratio of the HUSY zeolite increased to approximately 23.5 (S-Table 1). The increase in SiO_2/Al_2O_3 molar ratio was clearly more pronounced during acid treatment than the ion-exchange process, indicating greater removal of aluminum during the citric acid treatment than during the ion-exchange process and stabilization of the Y zeolite due to aluminum removal. Due to continuous dealumination, the HY zeolite first treated by citric acid and then ion-exchanged in NH_4NO_3 aqueous solution exhibited an even higher SiO_2/Al_2O_3 molar ratio than the other materials. The intensity of the diffraction peaks and crystallinity of the Y zeolites decreased as the SiO_2/Al_2O_3 molar ratio increased, indicating that during the dealumination, their crystallinity decreased. The intensities of the diffraction peaks of the different gallium-modified HUSY zeolites were slightly lower than for HUSY, implying a slight decrease in crystallinity during modification. In addition, the framework SiO_2/Al_2O_3 molar ratio increased slightly as the gallium content increased, indicating that a small amount of framework aluminum was have been replaced by gallium species and some framework aluminum became non-framework Al species during the modification.

Gallium was deposited onto the HUSY zeolite to obtain modified zeolites with detected amounts of 1.26, 2.03 and 2.87 wt.% G_2O_3. The mesoporous surface area and pore volume of the

10.1002/chem.201701307

modified zeolites were substantially retained upon metal incorporation (Table 1), perhaps due to the rather low loading. However, the microporous surface area and pore volumes of the zeolites decreased as the incorporation of gallium increased. Although XRD analysis (Fig. 1) indicated a slight decrease in crystallinity (Table 1), the absence of reflections specific to Ga_2O_3 in the patterns suggested the presence of a well-dispersed, nanostructured gallium phase. It is possible that the pore structure of the USY zeolite underwent a small degree of destruction after modification by gallium (Fig. 1) and that some portion of the micro pores were blocked by the introduced gallium species and removed aluminum (Table 1). To further confirm the positions of the introduced gallium species on HUSY zeolites, the XPS spectra of Ga 3d for each modified zeolite were recorded (Fig. 2). The XPS spectra of Si 2p and Al 2p for 2GaHUSY were also recorded (S2).

Based on the results presented in Fig. 2, we can conclude that there are four peaks at binding energies of 21.4 eV, 24.7 eV, 26.0 eV and 27.2 eV that correspond to Ga_2O_3 species, Ga-O(H)-Al bonds, Ga-O(H)-Si bonds and Ga-OH species, respectively[31,37]. When the content of gallium is relatively low, the main gallium species is Ga-O(H)-Al, and as the content of gallium increases, the presence of Ga_2O_3 and Ga-O(H)-Si increases. The result presented in S2A exhibits a peak at the binding energy of 99.8 eV, which was attributed to the Si-O(H)-Ga bonds, and the result presented in S2B exhibits a peak at the binding energy of 72.6 eV, which was attributed to the Al-O(H)-Ga bonds[29,31,37]. All these results indicate that gallium species exhibit a preference to coordinate with Al species or substitute the Al-OH groups in zeolites during the modification process and the preference for Al diminishes for an increase of Ga loading.

3.2 Acidity properties

10.1002/chem.201701307

Acidity plays an important role in the formation of the active phase and the HDS reaction[38], and the acidities of all modified HUSY zeolites and the corresponding catalysts were investigated using NH_3-TPD and Py-FTIR methods, respectively. Fig. 3 shows the NH_3-TPD profiles of the modified HUSY zeolites and the catalysts. The NH_3-TPD profiles in Fig. 3A reveal two NH_3 desorption peaks for gallium-modified HUSY at approximately 510 K and 680 K, indicating the presence of two types of acid sites with different acid strengths. In general, the NH_3 desorption peak at 510 K reveals the existence of weak acid sites, whereas the NH_3 desorption peak at 680 K indicates the existence of medium and strong acid sites. As the gallium content increased, the lower-temperature desorption peak for gallium-modified HUSY shifted slightly to an even lower temperature, suggesting that the acidity of the weak acid sites was weakened. The intensity of the lower-temperature desorption peak also decreased, indicating that the amount of weak acid sites decreased. The higher-temperature desorption peak also shifted to a lower temperature, but the intensity of the higher-temperature desorption peak increased, indicating a decrease in acid strength and an increase in the amount of medium and strong acid sites. The NH_3-TPD profiles in Fig. 3B reveal more than two peaks for the catalysts at temperatures of 495 K and higher, indicating the presence of complex acid types with different acid strengths. As the gallium content increased, the lower NH_3 desorption peak shifted to an even lower temperature, suggesting a decrease in the acid strength of the weak acid sites[39]. However, the other NH_3 desorption peak shifted to higher temperatures, suggesting an increase in the acid strength of the stronger acid sites. These results are similar to the observations of Meng et al.[40] over Y/ASA composite. They stated that a particular conjunction of the tetrahedrons and thus a special skeleton structure might be formed at the interface of the Y zeolite and ASA phases in the Y/ASA composite.

10.1002/chem.201701307

To observe the changes in Brønsted acid sites (BAS) and Lewis acid sites (LAS) on the modified HUSY zeolites and the corresponding catalysts, Py-FTIR spectrum analyses and pyridine desorption FTIR analyses were performed at different temperatures. The results are summarized in Table 2 and S3A~S3F. Compared to the acidity properties of HUSY, the amount of weak BAS decreased sharply as the gallium content increased, and the amount of weak LAS decreased slightly (473 K). The amount of medium BAS increased obviously after gallium modification, and 2GaHUSY contained the most medium BAS (553 K). However, the medium LAS decreased slightly. The data in Table 2 demonstrate that both strong BAS and strong LAS (623 K) decreased proportionally as the gallium content increased. In addition, the total amounts of BAS and LAS decreased with increasing gallium content, and the B/L ratio increased. Similar trends were observed for the corresponding catalysts. Moreover, there is an interesting result showing that the total amounts of BAS decreased from 680 to 539 μmol g^{-1} as the gallium content increased from 0 to 3 wt.%, and the trend became more pronounced. Regarding the total amounts of LAS, a slower downtrend was first observed, and afterward, the trend reversed to an uptrend as the gallium content increased from 2 wt.% to 3 wt.%.

3.3 H_2-TPR measurement

The H_2-TPR technique can effectively characterize the reducibility of metal oxides loaded on a support. Fig. 4 presents the H_2-TPR profiles for the investigated catalysts. Octahedrally coordinated MoO_3 species can be reduced at temperatures from approximately 600 K to 900 K, when loaded on a support. Hexa-coordinated Mo(Ⅳ) species are formed that have strong interactions with supports and thus are harder to reduce and often require higher temperatures, from approximately 900 K to 1100 K [14,41,42]. The H_2-TPR profiles displayed in Fig. 4 revealed

10.1002/chem.201701307

two main H_2 consumption peaks centered at temperatures of approximately 730 K and 1030 K. The H_2 consumption peak at 730 K can be attributed to the reduction of higher coordinated MoO_3 species to lower coordinated Mo(Ⅳ) species, and the H_2 consumption peak shouldered at 1030 K can be ascribed to the reduction of tetra-coordinated Mo(Ⅳ) species, which are difficult to reduce due to their strong interaction with the supports. The reduction peaks of Ni species are probably masked by the MoO_3 reduction peaks. Compared to NiMo/Y-ASA-A, the H_2-TPR profiles of the catalysts containing gallium-modified HUSY zeolites exhibited a significant change: the two reduction peaks notably shifted to lower temperatures, indicating that the reducibility of Mo species on these catalysts clearly improved. Moreover, the peak area at the lower temperature increased, and the peak area at the higher temperature decreased. However, when the gallium content was increased to 3 % in the modified zeolite, the H_2-TPR profile presented three reduction peaks. The peak centered at 550 K is attributable to the reduction of Ga_2O_3 to Ga_2O[31]. Compared with NiMo/2GaY-ASA-A, the Mo peak of NiMo/3GaY-ASA-A at lower temperature shifted slightly to a higher temperature, and the Mo peak at higher temperature shifted to an even higher temperature, suggesting that the reducibility of the Mo species on NiMo/3GaY-ASA-A was slightly deteriorated compared with NiMo/2GaY-ASA-A. These results can be explained by the theory proposed in the literatures elsewhere[28,29] that the existence of gallium in tetrahedral coordination over the aluminum sites, which results in the decrease of aluminum sites at the surface of USY zeolites and leads to a decrease in the formation of Mo-O-Al bonds, which is considered to be the real mode of the interaction between active metals and supports, thus the interaction decreased.

3.4 HRTEM results

10.1002/chem.201701307

HRTEM studies were performed to compare the sulfide metal dispersion degree of the investigated catalysts. Fig. 5 displays the representative micrographs taken from different catalysts. The statistical analyses of the average slab length and stacking layers of active MoS_2 slabs over sulfide catalysts were obtained by counting at least 500 slabs obtained from different parts of each catalyst. The average length $\bar{L}$ and stacking number $\bar{N}$ were calculated according to Eq. 1 and Eq. 2 and are listed in Table 3. A high dispersion of the active phase is necessary for the formation of large numbers of accessible active sites. Slabs with a shorter length and lower stacking number are beneficial for the formation of more CUS sites, namely "type Ⅱ" active phase[29,42]. However, when the stacking height of MoS_2 slabs is lower than the size of the aromatic ring, the planar adsorption of reactant molecules will be strictly limited, and the HDS activity of highly refractory sulfur-containing compounds will be constrained. Thus, we performed a more detailed comparison by calculating the MoS_2 dispersion f_{Mo} according to Eq. 3, and the calculated results are also listed in Table 3. The results demonstrate that both the average stacking number and the average length of MoS_2 slabs changed with the increased gallium content. For NiMo/ASA-A, the average length of the MoS_2 slabs was 5.3 nm, the average stacking number was 2.7, and there are a large proportion of monolayer MoS_2 slabs, which are less active for 4,6-DMDBT HDS reactions. When HUSY was added as a cosupport, the average length decreased to 5.1 nm, and the average stacking number increased to 3.5. More importantly, the amount of the less active monolayer MoS_2 slabs decreased to a relatively small proportion. When the HUSY zeolites were modified by different contents of gallium, the average length further decreased, the average stacking number further increased with increasing gallium content, and the monolayer MoS_2 slabs nearly disappeared from view. However, when the gallium content increased to 3wt.%, this trend was

reversed, especially for the amount of monolayer MoS_2 slabs and the average length. The dispersion and stacking of MoS_2 slabs may have been improved on HUSY zeolites, and the introduced gallium caused a clear decrease in the interaction of the active MoS_2 species with the supports. The highest f_{Mo} (0.29) was obtained over NiMo/2GaY-ASA-A with an average length of 4.6 nm, an average stacking number of 3.8 and the smallest amounts of monolayer MoS_2 slabs. To visualize how Ga species influence the dispersion of Ni and Mo species over the sulfided catalysts, Ga, Ni and Mo elemental scanning images of the NiMo/Y-ASA-A and the NiMo/2GaY-ASA-A catalysts were obtained and the results are shown in S9 and S10. The results imply that after gallium modification, there are more Ni species embedded in Mo species which is beneficial for the formation of more NiMoS active phase. This is highly consistent with the results observed from HRTEM images and the results obtained from XPS characterization.

3.5 XPS results

To analyze the valence states of active metals and further investigate how the three metals (Ga, Ni and Mo) interact in the sulfided catalyst, the XPS characterization of the sulfided catalysts were carried out and the Mo 3d XPS spectra and the Ni 2p XPS spectra together with their deconvolution results for the investigated sulfided catalysts are shown in S6 and S7 and the details are summarized in Table 4. It can be seen that the sulfidation of Mo species($Mo_{sulfidation}$) increase in the order: NiMo/Y-ASA-A < NiMo/ASA-A < NiMo/1GaY-ASA-A < NiMo/2GaY-ASA-A < NiMo/3GaY-ASA-A and the sulfidation of Ni species($Ni_{sulfidation}$) increase in the order: NiMo/Y-ASA-A < NiMo/ASA-A < NiMo/1GaY-ASA-A < NiMo/3GaY-ASA-A < NiMo/2GaY-ASA-A, more importantly, the proportion of NiMoS species increase in the same order with the $Ni_{sulfidation}$. These results are consistent with the H_2-TPR of the oxide catalysts and

the HRTEM results of the sulfide catalysts. All these results are consistent with the results observed over NiMo/Ga-Al2O3 catalyst by E. Altamirano et al.[28,43], and their theory is that small amount of Ga causes a decrease in the interaction between support and active metal(decrease in the amounts of Mo-O-Al bonds and $NiAl_2O_4$ species). Due to its moderate interaction between active metals and the supports, NiMo/2GaY-ASA-A exhibits the highest Mo dispersion and the largest proportion of NiMoS species, which is considered as the real active phase of the non-noble metal hydrotreating catalysts.

3.6 4,6-DMDBT HDS results

4,6-DMDBT is the most commonly representative highly refractory organosulfur compound in inferior diesels. Thus, it is one of the most common probe molecules in the assessment of the HDS performance of hydrotreating catalysts. Fig. 6 displays the 4,6-DMDBT conversions over different catalysts at different LHSVs. The LHSV was varied in the range of 10 h^{-1} to 160 h^{-1} with a reaction temperature of 563 K, total pressure of 4 MPa and H_2/Oil ratio of 120:1. The results showed that NiMo/2GaY-ASA-A exhibited the highest 4,6-DMDBT conversion for all LHSVs. At 20 h^{-1}, the most representative LHSV of our system, NiMo/2GaY-ASA-A exhibited a 4,6-DMDBT conversion of 57.6 %, approximately 2 times the value for NiMo/ASA-A and approximately 1.3 times the value for of NiMo/Y-ASA-A. Fig. 6 also indicates that the gallium-modified catalysts exhibited higher 4,6-DMDBT conversion at all LHSVs.

To distinguish the different desulfurization routes and the contributions of each desulfurization route to the overall HDS performance over each investigated catalyst, we varied the LHSVs to control the total conversion of 4,6-DMDBT at approximately 50 % and analyzed the HDS products by GC-MS. The results are displayed in Table 5. Twelve types of products were detected

over catalysts containing Y zeolites, including the following: 4,6-tetrahydro-dimethyldibenzothiophene (4,6-THDMDBT) and 4,6-hexahydro-dimethyldibenzothiophene (4,6-HHDMDBT), which were identified as the intermediates of the HYD pathway; 3,3'-dimethylcyclohexylbenzene (3,3'-DMCHB) and 3,3'-dimethylbicyclohexyl (3,3'-DMBCH), which were identified as the desulfurized products of the HYD pathway; 3,3'-DMBP, which was identified as the product of the DDS pathway. Some other types of products, such as 3,4'-DMBP, which was observed for the first time in the HDS reaction of 4,6-DMDBT, 4,4'-DMBP, and a small proportion of iso-methyl-isopropyltetralin (Iso-MIPT)[4], which were identified as the products of the isomerization (ISO) pathway, were also detected over zeolite-containing catalysts (Fig. 7A). More importantly, 3,6-DMDBT and 3,7-DMDBT, two isomers of 4,6-DMDBT, were also observed based on the GC peaks with retention times of approximately 20.2 min and 20.6 min (Fig. 7B), which indicates that 4,6-DMDBT first underwent methyl migration to form 3,6-DMDBT and 3,7-DMDBT before S atom removal. Moreover, tri- and tetra-methyl-DBTs were also detected based on the two GC peaks with retention times of 21.5 and 24.7 min (Fig. 7B and S5). These results indicate that the transmethylation (TRM) of methyl groups between different 4,6-DMDBT molecules also occurred over zeolite-containing catalysts before desulfurization. However, only five types of products, 4,6-THDMDBT, 4,6-HHDMDBT, 3,3'-DMDBT, 3,3'-DMCHB and 3,3'-DMBCH, were observed over NiMo/ASA-A, indicating that 4,6-DMDBT only underwent HYD and DDS over NiMo/ASA-A during the hydrotreating process due to the lack of medium and strong Brønsted acid sites. This result demonstrates that Brønsted acidity, especially medium and strong Brønsted acidity from the acidic cosupports, plays a very important role in the HDS activity of 4,6-DMDBT,

especially in the selectivity of its HDS pathway. The main product of 4,6-DMDBT HDS over NiMo/ASA-A was 3,3'-DMCHB, and the HYD pathway selectivity reached as high as 82 %, indicating that 4,6-DMDBT was mainly transformed by the HYD pathway over nonacidic catalysts, which shows good consistency with the results reported elsewhere in the literature[4,9,11].

However, the main products of 4,6-DMDBT HDS over gallium-modified HUSY zeolite-containing catalysts were 3,4'-DMBP and 4,4'-DMBP and ISO-MIPT, indicating that 4,6-DMDBT was mainly transformed through the ISO pathway over acidic catalysts. Moreover, the selectivity of 3,4'-DMBP and 4,4'-DMBP increased with the amount of medium Brønsted acid sites and reached 45 % over NiMo/2GaY-ASA-A. The total isomerization selectivity also increased with the amount of medium Brønsted acid sites and reached 59 % over NiMo/2GaY-ASA-A. Furthermore, the selectivity of tri- and tetra-methyl-DBTs decreased with the amount of strong Brønsted acid sites from 13 % over NiMo/Y-ASA-A to 4 % over NiMo/2GaY-ASA-A and NiMo/3GaY-ASA-A. The total DDS reaction selectivity increased from 18 % over NiMo/ASA-A to 38 % over NiMo/Y-ASA-A, and then to 54 % over NiMo/2GaY-ASA-A.

To further confirm each of the 4,6-DMDBT HDS pathways and the isomerization and the transmethylation abilities of each catalysts, the global rate constant (k_{HDS}) of the 4,6-DMDBT HDS reactions were calculated using Eq. 4. The rate constants of each 4,6-DMDBT HDS pathway were also calculated. The results are listed in Table 5. All the rate constants were calculated by varying the LHSV in the range of 10 h^{-1} to 160 h^{-1} with the other reaction conditions fixed. To further compare the performance of each catalyst for the 4,6-DMDBT HDS reaction, the

activation energies of each catalyst at 563 K were calculated according to Eq. 6 by testing reaction temperatures of 558 K and 573 K with an LHSV of 40 h^{-1} and the other conditions fixed as described earlier. The results are also listed in Table 5.

The kinetic study results in Table 5 show that the overall activation energies of the 4,6-DMDBT HDS reaction decreased from 208 KJ mol^{-1} to 159 KJ mol^{-1} after the addition of 10 wt.% HUSY zeolite. Moreover, the activation energies further dropped with increasing gallium modification content to a minimum value of 134 KJ mol^{-1} over NiMo/2GaY-ASA-A, and then this trend slightly reversed. Otherwise, the global rate constant of the 4,6-DMDBT HDS reaction (k_{HDS}) increased from $2.8*10^{-4}$ mol g^{-1} h^{-1} to $6.1*10^{-4}$ mol g^{-1} h^{-1} after the addition of acidic cosupport and further increased to $8.1*10^{-4}$ mol g^{-1} h^{-1} over NiMo/2GaY-ASA-A, then dropped slightly to $7.8*10^{-4}$ mol g^{-1} h^{-1} over NiMo/3GaY-ASA-A. These results indicated that catalysts containing HUSY zeolites exhibited higher activity than NiMo/ASA-A, and NiMo/2GaY-ASA-A exhibited the highest activity for the 4,6-DMDBT HDS reaction. The reaction rate constants of each 4,6-DMDBT HDS pathway were also calculated at a 4,6-DMDBT conversion of approximately 50 %, and the results are also shown in Table 6. The results showed that the rate constant of HYD pathway increased slightly after the addition of acidic cosupport and then remained almost the same with increased gallium content on HUSY zeolites; however, the total rate constant of the DDS pathway over the zeolites containing catalysts was almost 4.5 times the level of NiMo/ASA-A, remained almost unchanged before the acidic cosupports were modified by gallium, then increased to approximately 9 times the value of NiMo/ASA-A over NiMo/2GaY-ASA-A. The most obvious change was observed over the ISO pathway and TRM pathway, which were only observed over the zeolite-containing catalysts, indicating that the acidity of the acidic cosupports plays an

important role in the reaction pathways of the 4,6-DMDBT HDS process. For the isomerization(ISO) pathway, the rate constant increased from $2.3*10^{-4}$ mol g^{-1} h^{-1} over NiMo/Y-ASA-A to $4.8*10^{-4}$ mol g^{-1} h^{-1} over NiMo/2GaY-ASA-A, then decreased slightly to $4.5*10^{-4}$ mol g^{-1} h^{-1} over NiMo/3GaY-ASA-A. For the transmethylation (TRM) pathway, the rate constant decreased from $0.8*10^{-4}$ mol g^{-1} h^{-1} over NiMo/Y-ASA-A to approximately $0.3*10^{-4}$ mol g^{-1} h^{-1} over NiMo/2GaY-ASA-A and NiMo/3GaY-ASA-A. The ISO pathway selectivity (k_{ISO}/k_{HDS}) values over different catalysts were also calculated, and the results showed an increased from 0.37 over NiMo/Y-ASA-A to approximately 0.6 over NiMo/2GaY-ASA-A and NiMo/3GaY-ASA-A.

4. Discussion

4.1 Effect of gallium modification on catalyst properties

The XRD patterns revealed that gallium modification caused a slight decrease in crystallinity (Fig. 1 and S-Table 1) due to the impregnation of gallium species, and from the XPS results of the Ga 3d spectra for modified HUSY zeolites (Fig. 2), we can conclude that most of the gallium species were introduced into the Y zeolite framework through the formation of Ga-O(H)-Al bonds (framework substitution at the zeolite surface) and Ga-O(H)-Si bonds (framework substitution at the zeolite surface) [44-47]. Moreover, the XPS spectra also indicated that the Ga_2O_3 species was formed with the increase of gallium modification content (Fig. 2), thus decreasing the crystallinity. The micropore surface area and pore volume of the modified zeolites decreased with increasing gallium content, but the mesopore surface area was maintained (Table 1), indicating that the Ga-species plugged some micropores. However, the decrease in pore diameter (Table 1) indicated that most Ga-species were located on the mesopore surface of HUSY crystals to form Ga-O(H)-Al

bonds. Moreover, Johnson et al.[48] stated that the acidic properties of the support were an important factor in determining metal dispersion. The dispersion of the metal atoms on the support increased with higher concentrations of acid sites, particularly the strong acid sites present in steamed zeolite HY. In our case, the amounts of both strong BAS and strong LAS decreased with increasing gallium content because the strong acid sites on the mesopore surface and external surface or even in super cages of zeolites were covered by gallium species, as evidenced by the fact that most of the introduced gallium species existed as Ga-O(H)-Al. The amount of medium LAS decreased, while the amount of medium BAS increased with gallium content. The largest amount of medium BAS and the smallest amount of medium LAS were obtained when the gallium content was 2 wt.%. This result indicates that gallium modification can lead to LAS transfer into BAS on HUSY zeolites at lower gallium content, but when the gallium content increases, the opposite transformation occurs (for 3GaHUSY). The total amount of acid sites decreased slightly before and after HUSY modification by a relative low content of gallium nitrite (1GaHUSY, Fig. 3A and Table 2), but with increasing gallium content, the amounts of both BAS and LAS declined, indicating that not only did the introduced gallium species replace some aluminum species to form Ga-O(H)-Al and Ga-O(H)-Si bonds on the mesopore surface and outer surface of HUSY, but based on the emergence of Ga-O-Ga bonds, bulky Ga_2O_3 also formed (Fig. 2). As mentioned earlier, the dispersion of metal atoms on the support increased at a higher concentration of acid sites, and gallium modification can cause variation of the acidity properties and textural properties of zeolites. For the corresponding catalysts, the strongest acid centers were covered by Ga_2O_3 or substituted by Ga-O(H)-Si sites, and because Ga-O(H)-Si sites are more covalent than Al-O(H)-Si sites[31,35,37], the interaction between the active phase and support was decreased. This decrease

can be explained by the fact that the average electronegativity value of 1.59 for Ga is lower than the value for Al (1.71), implying a lower acid strength of both Brønsted protons and Lewis caves for Ga-substituted zeolites. Thus, the reduction temperature of the catalysts decreased with the increase in gallium modification content, as observed from the H_2-TPR profiles (Fig. 4), which indicates that the interaction between the active metals and supports was weakened. The change in the acidic properties of the support should influence the distribution of active metals on the surface and thus affect the active phase in the catalyst grain. Moreover, the HRTEM results demonstrated that after gallium modification, the average length of the MoS_2 slabs decreased and the average stacking number of the MoS_2 slabs increased with increasing gallium content. The value of the Mo dispersion also increased with increasing gallium content and reached its highest value over NiMo/2GaY-ASA-A (Table 3). This phenomenon can be explained by the confinement effect from the highly dispersed Ga_2O_3 grains doped on the surface of HUSY zeolites. As the length of the MoS_2 slabs decreases and the stacking number increases, more highly active 'type Ⅱ Ni-Mo-S active phase' will be formed, which will favor both the adsorption and the conversion of 4,6-DMDBT.

4.2 Effect of gallium modification on the catalyst performance of 4,6-DMDBT HDS

The zeolite-containing catalysts, especially the gallium-modified zeolite-containing catalysts, exhibited much higher HDS activity than NiMo/ASA-A. Among all the prepared catalysts, NiMo/2GaY-ASA-A exhibited the highest 4,6-DMDBT conversion at 563 K at all LHSVs. This difference was mainly caused by the differences in the acidity properties of the supports and the differences in active metal morphology caused by the acidity properties. As reported by several researchers elsewhere, it has been confirmed that acidity, especially Brønsted acidity, plays an

important role in the activity of 4,6-DMDBT conversion[4,27]. Once protonized, the methyl groups at the 4 and 6 positions of 4,6-DMDBT can be eliminated or shifted away by dealkylation or isomerization, reducing the hindrance caused by these methyl groups reduced and rendering the subsequent conversion much easier. Pérot[2] and Bataille et al.[49] used Y zeolite as a component of their HDS catalyst and employed 4,6-DMDBT as a probe molecule in their study, observing some isomerized intermediates. A similar conclusion was drawn by Sun and Prins et al.[11] when they used another acidic zeolite, mesoporous ZSM-5, as support and 4,6-DMDBT HDS as a reaction probe: they observed tri-methyl-cyclopentenyl benzene as one of the HDS products and confirmed the existence of an isomerization pathway. Moreover, when they neutralized the acidity of ZSM-5 zeolite by piperidine, tri-methyl-cyclopentenyl benzene disappeared in the final HDS product, proving that the acidity of the supports determined the ISO pathway during the HDS of 4,6-DMDBT. Isoda et al.[50] observed that the methyl groups at the 4 and 6 positions of 4,6-DMDBT could migrate to the 3 and 7 positions on a Ni/Y catalyst, drastically decreasing the activation energy and making the HDS reaction much easier. Recently, Wu and Duan et al.[4] reported that 4,6-DMDBT can be transformed to 3,7-DMDBT over a NiMo hydrodesulfurization catalyst supported on an acidic zeolite containing micro-mesoporous composite zeolite. Moreover, they found that the isomerization selectivity corresponded to the quantity of Brønsted acid sites. The kinetic study showed that after the methyl groups at the 4 and 6 positions of 4,6-DMDBT were transferred to the 3 and 7 positions, the reactant molecule could be adsorbed on the active sites through both planar adsorption and σ-adsorption rather than only through planar adsorption for 4,6-DMDBT. Thus, the global reaction rate constant k_{HDS} of the zeolite-containing catalysts for the 4,6-DMDBT HDS reaction increased obviously, and the activation energies of the

10.1002/chem.201701307

4,6-DMDBT HDS reaction dropped drastically after the addition of acidic zeolites (Table 6). As described earlier, the cleavage of the C-S bond is favored by σ-adsorption, and thus it is much easier for 3,6- and 3,7-DMDBTs to undergo DDS route than for 4,6-DMDBT over hydrotreating catalysts. In addition, in this work, we observed that the ISO selectivity is closely related to the total number of medium and strong Brønsted acid sites, while the TRM selectivity is only closely related to the number of strong Brønsted acid sites. As shown in Fig. 8, the ISO selectivity and the number of medium and strong Brønsted acid sites exhibit similar trends, as do the TRM selectivity and the number of strong Brønsted acid sites. Based on this theory, NiMo/2GaY-ASA-A exhibits the largest total number of medium and strong Brønsted acid sites (Table 2), and thus 4,6-DMDBT can be easily transformed to 3,6- and 3,7-DMDBT, which can then easily produce 3,4'-DMBP and 4,4'-DMBP as the main products via the DDS pathway(Table 4). On the other hand, because NiMo/2GaY-ASA-A and NiMo/3GaY-ASA-A exhibit the lowest amounts of strong Brønsted acid sites, the smallest amounts of trimethyl- and tetramethyl-DBTs are produced. Since trimethyl- and tetramethyl-DBTs are even more refractory sulfur-containing compounds than 4,6-DMDBT and are even harder to transform into other products over hydrodesulfurization catalysts, the formation of these products should be avoided. NiMo/2GaY-ASA-A exhibits the highest 3,4'-DMDBT and 4,4'DMDBT selectivity and the lowest trimethyl- and tetramethyl-DBTs selectivity. As mentioned previously, considering the great similarity in chemical behavior between gallium and aluminum, Ga-OH-Si sites formed at the mesopore surface of the HUSY zeolite, and some Al-O(H)-Si sites were substituted by Ga-O(H)-Si/Al-O(H)-Ga sites (Fig. 2); Al-O(H)-Si sites were also formed at the interface of different components of the catalyst supports[51,52]. Thus, some L acid sites, together with some weak and strong B acid sites, were transformed into medium B acid sites

(Table 2)[53]. Although the gallium-modified zeolites have lower acid strength than the original zeolites, it is easier for gallium-modified zeolites to donate Brønsted protons. Therefore, gallium modification can improve the reaction rate of the ISO route (highest k_{ISO} value and isomerization selectivity in Table 6) and suppress the reaction rate of the TRM route (lowest k_{TRM} in Table 6), ultimately enhancing the HDS of 4,6-DMDBT.

The reaction network including the HYD and DDS pathways for 4,6-DMDBT over commercial NiMo/Al_2O_3 has been studied extensively[19,23,40]. It is widely accepted that in the HYD pathway, 4,6-DMDBT first undergoes a hydrogenation process to produce 4,6-THDMDBT, which is immediately transformed to 4,6-HHDMDBT; then, one S atom is removed to form 3,3'-DMCHB; or the 4,6-HHDMDBT further hydrogenated to dodecahydro-DMDBT, which will be hydrogenated to 3,3'-DMBCH. By contrast, in the DDS pathway, the S atom is directly removed by breaking the C-S bond to produce 3,3'-DMBP. Due to its highly refractory nature and adsorption manner, 4,6-DMDBT HDS reaction mainly undergoes the HYD pathway over commercial NiMo/Al_2O_3 catalysts. In our case, the main product of 4,6-DMDBT HDS over NiMo/ASA-A is 3,3'-DMCHB, which was identified as the final product of the HYD pathway; 3,3'-DMBP, which was identified as the final product of the DDS pathway; and relatively small amounts of 4,6-THDMDBT and 4,6-HHDMDBT (Table 5), which were identified as the intermediates of the HYD pathway. This result is highly consistent with the results reported elsewhere in the literature[54]. The absence of ISO and TRM products proves that weak Brønsted acid sites do not contribute to the isomerization and transmethylation processes. However, the product distribution and kinetic behavior of 4,6-DMDBT HDS over the zeolite-containing catalysts was completely different, particularly over NiMo/2GaY-ASA-A; the main products were

3,4'- and 4,4'DMBP and 3,6- and 3,7-DMDBT, which were identified as the products and intermediates of the ISO pathway rather than 3,3'-DMCHB and 3,3'-DMBP. The high isomerization rate constant and ISO pathway selectivity (Table 6) over NiMo/2GaY-ASA-A confirmed that NiMo/2GaY-ASA-A exhibits a superior methyl group migration property. Based on the differences in product distribution, kinetic behavior and catalyst properties, we conclude that 4,6-DMDBT was first transformed to 3,6- and 3,7-DMDBT via an isomerization pathway over the medium and strong B acid sites, followed by removal of the sulfur atom to form 3,4'- and 4,4'-DMBP via the DDS pathway over the active sites of the catalysts. In the analysis of the HDS products of 4,6-DMDBT, tri- and tetra-methyl-DBTs were identified simultaneously (Fig. 7 and S5), and the amounts of these multi-methyl-DBTs were closely related to the number of strong B acid sites (Fig. 8). We therefore conclude that methyl migration is closely related to the Brønsted acidity of the hydrotreating catalysts and that the migration of methyl groups on the 4 and 6 positions of 4,6-DMDBT within one molecule (isomerization) is closely related to the amounts of medium and strong BAS, whereas the migration of methyl groups from one molecule to another (transmethylation) is closely related to the quantity of strong BAS.

To further understand the 4,6-DMDBT HDS over our catalysts, an overall new reaction network including the products and intermediates of the HYD, DDS, ISO and TRA pathways (Fig. 10) was proposed based on the kinetic behavior and product distribution. The HYD and DDS pathways of 4,6-DMDBT are the typical reaction pathways in the 4,6-DMDBT HDS over NiMo/ASA-A. The ISO and TRM pathways of the 4,6-DMDBT HDS reaction only occur over the zeolite-containing catalysts. In the DDS pathway, the S atom was directly removed by hydrogenolysis to produce 3,3'-DMBP as the product. In the HYD pathway, 4,6-DMDBT was first hydrogenated to

4,6-THDMDBT and 4,6-HHDMDBT, followed by the removal of the S atom to produce 3,3'-DMCHEB and 3,3'-DMCHB by DDS and hydrogenation. With a global reaction rate constant k_{HDS} of 2.8*10^{-4} mol^{-1} h^{-1} and k_{HYD} of 2.3*10^{-4} mol^{-1} h^{-1}, 4,6-DMDBT mainly underwent the HDS reaction through the HYD pathway over NiMo/ASA-A. In the ISO pathway, the main reaction pathway for 4,6-DMDBT HDS over acidic zeolite-containing catalysts, the methyl groups at the 4 or 6 position first shifted to the 3 or 7 position, which drastically decreased their steric hindrance (Fig. 9); subsequently, the S atom in the isomerized intermediate molecules was removed either through the HYD pathway or through the DDS pathways. The DDS pathway of 3,6-DMDBT and 3,7-DMDBT became the main reaction pathway, and thus 3,4'-DMBP and 4,4'-DMBP were the main products of 4,6-DMDBT HDS over NiMo/2GaY-ASA-A. The global reaction rate constant k_{HDS} of the 4,6-DMDBT HDS reaction increased from 6.1*10^{-4} mol^{-1} h^{-1} over NiMo/Y-ASA-A to 8.1*10^{-4} mol^{-1} h^{-1} over NiMo/2GaY-ASA-A, and the k_{ISO} of the ISO pathway increased from 2.3*10^{-4} mol^{-1} h^{-1} over NiMo/Y-ASA-A to 4.8*10^{-4} mol^{-1} h^{-1} over NiMo/2GaY-ASA-A, indicating that the increase in the global reaction rate constant k_{HDS} is mainly contributed by the increase in the rate constant of the ISO pathway, k_{ISO}, and thus the highest isomerization selectivity is observed over NiMo/2GaY-ASA-A. All these results indicate that 4,6-DMDBT underwent the HDS reaction mainly through the ISO pathway. In the TRM route, the methyl groups at the 4 or 6 positions of one 4,6-DMDBT molecule are transferred to another 4,6-DMDBT molecule over strong B acid sites to form trimethyl- and tetramethyl-DBTs, which exhibit even higher steric hindrance than 4,6-DMDBT. Although the ISO pathway of the 4,6-DMDBT HDS reaction was reported elsewhere in the literature[4], the ISO pathway proposed in our research is new and different. 3,4'-DMBP was observed as one of the most products and

detected for the first time, and, substantial amounts of two isomers of 4,6-DMDBT, the intermediates 3,6-DMDBT and 3,7-DMDBT, were detected simultaneously over NiMo/2GaY-ASA-A. In addition, the TRM route in our reaction network is new, and 3,4,6-TMDBT was identified for the first time in our research. Considerable amounts of trimethyl-DBT and tetramethyl-DBT were detected simultaneously in the HDS of 4,6-DMDBT over NiMo/2GaY-ASA-A. The ISO selectivity (59 %) over NiMo/2GaY-ASA-A was higher than for other zeolite-containing catalysts, whereas the TRM selectivity (4 %) of NiMo/2GaY-ASA-A was lower than for other zeolite-containing catalysts.

5. Conclusions

HUSY zeolites have been prepared and modified with different contents of gallium nitrite to adjust their acidity. 2GaHUSY exhibited the highest number of medium Brønsted acid sites due to the substitution of Al-OH-Si sites by Ga-OH-Si sites and the formation of Ga-OH-Al bonds in the modified samples. Thus, the corresponding catalyst, NiMo/2GaY-ASA-A, exhibited the highest k_{ISO} and k_{HDS} and the highest 4,6-DMDBT conversion at 563 K. Two isomers of 4,6-DMDBT, 3,6-DMDBT and 3,7-DMDBT, were detected simultaneously in the HDS products of 4,6-DMDBT over gallium-modified Y zeolite-containing catalysts. 3,4'-DMBP and 3,4,6-TMDBT were identified for the first time in the HDS products of 4,6-DMDBT over Y zeolite-containing HDS catalysts, and tetra-methyl-DBT was detected simultaneously. For the same reaction conditions, the 4,6-DMDBT conversion over NiMo/2GaY-ASA-A was approximately double the conversion over NiMo/ASA-A and approximately 1.2 times the conversion over NiMo/Y-ASA-A. The 4,6-DMDBT HDS reaction rate constant was approximately triple the value for NiMo/ASA-A and approximately 1.3 times the value for NiMo/Y-ASA-A; more importantly, the isomerization

reaction rate constant was approximately double the value for NiMo/Y-ASA-A, and the 4,6-DMDBT isomerization selectivity could reach approximately 60 % over NiMo/2GaY-ASA-A. This result suggested that the reaction of 4,6-DMDBT HDS over Y zeolite-containing catalysts followed a different reaction network from over NiMo/ASA-A. The reaction network for the HDS of 4,6-DMDBT over NiMo/2GaY-ASA-A includes 4 pathways: DDS, HYD, ISO and TRM. The former two were as described in the literature[4,11-16], whereas the ISO pathway was the main reaction route over NiMo/2GaY-ASA-A, with 3,4'-DMBP and 4,4'-DMBP as its main products. The TRM reactions also occurred over NiMo/2GaY-ASA-A, with 3,4,6-TMDBT and tetra-methyl-DBT as products that are even more refractory than 4,6-DMDBT. In the latter two pathways, 4,6-DMDBT was isomerized over the medium and strong Brønsted acid sites of NiMo/2GaY-ASA-A, and the transmethylation process occurred over the strong Brønsted acid sites of NiMo/2GaY-ASA-A. Thus, the activation energies of 4,6-DMDBT HDS over NiMo/2GaY-ASA-A clearly declined and the reaction rate constant over NiMo/2GaY-ASA-A obviously increased compared to NiMo/ASA-A and NiMo/Y-ASA-A. Due to its high isomerization selectivity and low transmethyl selectivity, the catalytic activity of 4,6-DMDBT HDS was greatly enhanced.

Acknowledgements

The authors acknowledge the financial supports from the Union Fund of Natural Science Foundation of China and CNPC (Grant No. U1362203 and No. U1462117).

References

[1] C. Song, X. Ma, Appl. Catal. B 41 (2003) 207.

[2] L. Wang, Y. Zhang, Y. Zhang, Z. Jiang, C. Li, Chem.-Eur. J. 15 (2009) 12571.

[3] P. Wu, W. Zhu, A. Wei, B. Dai, Y. Chao, C. Li, H. Li, S. Dai, Chem.-Eur. J. 21 (2015) 15421.

[4] H. Wu, A. Duan, Z. Zhao, T. Li, R. Prins, J. Catal. 317 (2014) 303.

[5] C.S. Shalaby, S.K. Saha, X. Ma, C. Song, Appl. Catal. B 101 (2011) 718.

[6] O.Y. Gutiérrez, S. Singh, E. Schachtl, J. Kim, E. Kondratieva, J. Hein, J.A. Lercher, ACS Catal. 4 (2014) 1487.

[7] A. Olivas, T.A. Zepeda, Catal. Today 143 (2009) 120.

[8] T.A. Zepeda, B. Pawelec, J.L.G. Fierro, T. Halachev, J. Catal. 242 (2006) 254.

[9] X. Tao, Y. Zhou, Q. Wei, G. Yu, Q. cui, J. Liu, T. Liu, Fuel Process. Technol. 118 (2014) 200.

[10] W. Fu, L. Zhang, T. Tang, Q. Ke, S. Wang, J. Hu, G. Fang, J. Li, F.S. Xiao, J. Am. Chem. Soc. 133 (2011) 15346.

[11] Y. Sun, R. Prins, Angew. Chem. Int. Ed. 47 (2008) 8478.

[12] T. Tang, L. Zhang, W. Fu, Y. Ma, J. Xu, J. Jiang, G. Fang, F.S. Xiao, J. Am. Chem. Soc. 135 (2013) 11437.

[13] J. H. Kim, X. Ma, C. Song, Y. Lee, S. T. Oyama. Energy and Fuels, 19 (2005) 353.

[14] Z. Vít, L. Kaluža, D. Gulkuvá, Fuel, 15 (2014) 86.

[15] N. Bejenaru, C. Lancelot, P. Blanchard, C. Lamonier, L. Rouleau, E. Payen, F. Dumeignil, S. Royer, Chem. Mater. 21 (2009) 522.

[16] C. Song, K.M. Reddy, Appl. Catal. A 176 (1999) 1.

[17] O. Gutiérrez, T. Klimova, J. Catal. 281 (2011) 50

[18] R. Colman, M. Baldanza, M. Schmal, J. Phys. Chem. C 114 (2010) 18501.

[19] D. Zhang, A. Duan, Z. Zhao, C. Xu, J. Catal. 274 (2010) 273.

[20] A. Burton, K. Ong, T. Rea, I. Chan, Micropor. Mesopor. Mater. 117 (2009) 75.

[21] H. Zhang, Y. Ma, K. Song, Y. Zhang, T. Tang, J. Catal. 302 (2013) 115.

[22] K. Möller, B. Yilmaz, R. Jacubinas, U. Müller, T. Bein, J. Am. Chem. Soc. 133 (2011) 5284.

[23] B. Pawelec, J. Fierro, A. Montesinos, T.A. Zepeda, Appl. Catal. B, 80 (2008) 1.

[24] Q. Cui, Y. Zhou, Q. Wei, X. Tao, G. Yu, Y. Wang, J. Yang, Energy Fuels, 26 (2012) 4664.

[25] Z. Vít, D. Gulkuvá, L. Kaluža, S. Bakardieva, Marta Boaro, Appl. Catal. B 100 (2010) 463.

[26] J. Kim, C. Kim, N. Heo, W. Lim, K. Seff, J. Phys. Chem. C, 114 (2010) 15741.

[27] P. Dapsens, B. Kusema, C. Mondelli, J. Pérez-Ramírez, J. Mol. Catal. A, 388 (2014) 141.

[28] E. Altamirano, J.A. de los Reyes, F. Murrieta, M. Vrinat, J. Catal., 235 (2005) 403.

[29] J.N. Díaz de León, M. Picquart, M. Villarroel, M. Vrinat, F.J. Gil Llambias, F. Murrieta, J.A. de los Reyes, J. Mol. Catal. A, 323 (2010) 1.

[30] L.H. Vieira, K.T.G. Carvalho, E.A.U. González, S.H. Pulcinelli, C.V. Santilli, L. Martins, J. Mol. Catal. A, 422 (2016) 148.

[31] R. Fricke, H. Kosslick, G. Lischke, M. Richter, Chem. Rev. 100 (2000) 2345.

[32] K.E. Ogunronbi, N.A. Yassir, S.A. Khattaf, J. Mol. Catal. A, 406 (2015) 1.

[33] H. Nur, Z. Ramli, J. Efendi, A.N.A. Rahman, S. Chandren, L. Yuan, Catal. Comm. 12 (2011) 822.

[34] D. Zuo, M. Vrinat, H. Nie, F. Maugé, Y. Shi, M. Lacroix, D. Li, Catal. Today, 93-95 (2001) 751.

[35] A. Alsalme, N. Alzaqri, A. Alsaleh, M. Rafiq, H. Siddiqui, A. Alotaibi, E. Kozhevnikova, I. Kozhevnikov, Appl. Catal. B, 182 (2016) 102.

[36] S. Kasztelan, H. Toulhoat, J. Grimblot, J. Bonnelle, Appl. Catal. 13 (1984) 127.

[37] R. Carli, C.L. Bianchi, Appl. Surf. Sci. 74 (1994) 99.

[38] H. Kim, N. Jeong, K. Yoon, J. Am. Chem. Soc. 133 (2011) 1642

[39] D. Murzin, B. Kusema, E. Murzina, A. Aho, N. Tokarev, A. Boymirzaev, J. Wärnå, P. Dapsens, C. Mondelli, J. Ramírez, J. Catal. 330 (2015) 93.

[40] Q. Meng, B. Liu, J. Piao, Q. Liu, J. Catal. 290 (2012) 55.

[41] W. Chen, K. Sasaki, C. Ma, A. Frencel, N. Marinkovic, J. Muckerman, Y. Zhu, R. Adzic, Angew. Chem. Int. Ed. 57 (2012) 6131.

[42] R. Sign, D. Kunzru, S. Sivacumar, Appl. Catal. B, 185 (2016) 163.

[43] E. Altamirano, J.A. de los Reyes, F. Murrieta, M. Vrinat, Catal. Today, 133-135 (2008) 292.

[44] J. Li, Y. Yu, X. Li, W. Wang, G. Yu, S. Deng, J. Huang, B. Wang, Y. Wang, Appl. Catal. B. 172-173 (2015) 154.

[45] K. Karim, J. Dwyer, Appl. Catal. A, 109 (1994) 235.

[46] E.F. Iliopoulou, S.D. Stefanidis, K.G. Kalogiannis, A. Delimitis, A.A. Lappas, K.S. Triantafyllidis, Appl. Catal. B, 127 (2012) 281.

[47] B. Sulikowski, Z. Olejniczak, V.C. Corberán, J. Phys. Chem., 100 (1996) 10323.

[48] G.R. Johnson, A.T. Bell, J. Catal., 338 (2016) 264.

[49] F. Bataille, J. Lemberton, G. Pérot, P. Leyrit, T. Cseri, N. Marchal, S. Kasztelan, Appl. Catal. A, 220 (2001) 191.

[50] T. Isoda, S. Nagao, X. Ma, Y. Korai, I. Mochida, Energy Fuel 10 (1996) 1078.

[51] K. Almajnouni, N. Hould, W. Lonergan, D. Vlachos, R. Lobo, J. Phys. Chem. C, 114 (2010) 19395.

[52] X. Su, G. Wang, X. Bai, W. Wu, L. Xiao, Y. Fang, J. Zhang, Chem. Eng. J. 293 (2016) 365.

10.1002/chem.201701307

[53] M. Hunger, J. Weitkamp, Angew. Chem. Int. Ed. 40 (2001) 2954.

[54] H. Wang, R. Prins, J. Catal., 264 (2009) 31.

10.1002/chem.201701307

Tables and Figures

Table 1

Textural properties of the synthesized and modified zeolites.

Materials	S_{meso}(m^2g^{-1})	S_{micro}[a] (m^2g^{-1})	V[a] (cm^3g^{-1})	Pore diameter[b] (nm)	SiO_2/Al_2O_3[c]	Ga content[d] (wt.%)	Cryst.[e] (%)
NaY	--	763	0.43	2.24	5.8	--	100
HY	85	618	0.40	2.41	12.5	--	93
USY	118	597	0.36	2.72	14.9	--	92
HUSY	134	553	0.37	2.85	23.5	--	88
1GaHUSY	136	515	0.36	2.78	23.8	1.26	86
2GaHUSY	134	506	0.36	2.74	23.9	2.03	85
3GaHUSY	133	499	0.35	2.68	24.0	2.97	85

[a] Determined by the BET and the t-plot method.

[b] Calculated using the BJH method.

[c] Derived from XRD.

[d] Determined by ICP-AES.

[e] Derived from XRD using pure SiO_2 powder as inner standard agent.

10.1002/chem.201701307

Table 2

Textural and acidity properties of the zeolites and catalysts.

Materials	S_{BET}[a] (m^2g^{-1})	BAS[b] (μmol g^{-1})			LAS[b] (μmol g^{-1})			NiO content[c] (wt.%)	MoO3 content[c] (wt.%)
		473 K	553 K	623 K	473 K	553 K	623 K		
HUSY	687	438.5	156.6	86.4	463.4	198.5	89.3	--	--
1GaHUSY	651	374.4	245.8	52.7	438.4	142.8	34.8	--	--
2GaHUSY	640	316.7	273.2	36.9	415.8	116.2	16.2	--	--
3GaHUSY	632	289.3	218.9	32.4	443.9	140.3	7.6	--	--
NiMo/Y-ASA-A	232	152.6	44.8	23.7	238.2	86.8	76.7	4.6	14.5
NiMo/1GaY-ASA-A	238	148.3	89.5	16.6	213.9	74.5	35.1	4.7	14.6
NiMo/2GaY-ASA-A	244	147.1	98.4	9.5	188.5	56.4	18.6	4.8	14.6
NiMo/3GaY-ASA-A	240	145.5	92.6	11.4	207.6	73.9	13.8	4.6	14.6
NiMo/ASA-A	188	38.4	7.4	3.1	318.3	76.4	53.9	4.7	14.7

[a] Determined by the BJH method.

[b] Derived from Pyridine-FTIR.

[c] Determined by ICP-AES.

10.1002/chem.201701307

Table 3

Average length, layer number and f_{Mo} of MoS_2 slabs of all catalysts.

	NiMo/ASA-A	NiMo/Y-ASA-A	NiMo/1GaY-ASA-A	NiMo/2GaY-ASA-A	NiMo/3GaY-ASA-A
Average length (nm)	5.3	5.1	4.8	4.6	4.7
Average layer number	2.7	3.5	3.7	3.8	3.9
f_{Mo}	0.20	0.24	0.26	0.29	0.27

Table 4

XPS parameters of Mo 3d and Ni 2p contributions over the sulfided NiMo catalysts.

	NiMo/ASA-A	NiMo/Y-ASA-A	NiMo/1GaY-ASA-A	NiMo/2GaY-ASA-A	NiMo/3GaY-ASA-A
Mo^{4+}(%)	66	58	74	79	82
Mo^{5+}(%)	7	9	4	4	3
Mo^{6+}(%)	27	33	22	17	15
NiSx(%)	41	41	37	29	34
NiMoS(%)	49	46	56	68	61
NiO(%)	10	13	7	3	5
S_{Mo}[a](%)	66	58	74	79	82
S_{Ni}[b](%)	90	87	93	97	95

[a] $S_{Mo}=Mo_{sulfidation}= Mo^{4+}/(Mo^{4+} +Mo^{5+} +Mo^{6+})$

[b] $S_{Ni}=Ni_{sulfidation}=(NiSx+NiMoS)/(NiSx+NiMoS+NiO)$

10.1002/chem.201701307

Table 5

Product distribution for HDS of 4,6-DMDBT over different catalysts.

Catalysts	product selectivity (%)[a]							
	HYD			DDS	ISO			TRA
	4,6-THDMDBT	3,3'-DMCHB	3,3'-DMBCHP	3,3'-DMBP	3,4'-DMBP	Iso-MIPT[b]	3,6-DMDBT	TriMDBT
	4,6-HHDMDBT			4,4'-DMBP(DDS)		(HYD)	3,7-DMDBT	TetraMDBT
NiMo/ASA-A	2	67	13	18	0	0	0	0
NiMo/Y-ASA-A	3	32	3	12	26	6	5	13
NiMo/1GaY-ASA-A	3	26	3	10	34	4	11	8
NiMo/2GaY-ASA-A	4	21	3	9	45	5	9	4
NiMo/3GaY-ASA-A	3	22	4	9	43	5	10	4

[a] Determined at approximately 50 % total 4,6-DMDBT conversion by changing LHSV.

[b] Determined by the method reported.

10.1002/chem.201701307

Table 6

The catalytic performances for HDS of 4,6-DMDBT over various catalysts.

Cats	Ea (kJ mol^{-1})	k_{HDS} (10^{-4} mol g^{-1} h^{-1})	k_{HYD} (10^{-4} mol g^{-1} h^{-1})	k_{DDS} (10^{-4} mol g^{-1} h^{-1})	k_{ISO} (10^{-4} mol g^{-1} h^{-1})	k_{TRM} (10^{-4} mol g^{-1} h^{-1})	k_{ISO}/k_{HDS}
NiMo/Y-ASA-A	159	6.1	2.7	2.3	2.3	0.8	0.38
NiMo/1GaY-ASA-A	142	7.1	2.9	3.1	3.5	0.6	0.49
NiMo/2GaY-ASA-A	134	8.1	2.7	4.4	4.8	0.3	0.59
NiMo/3GaY-ASA-A	137	7.8	2.7	4.1	4.5	0.3	0.58
NiMo/ASA-A	208	2.8	2.3	0.5	--	--	--

10.1002/chem.201701307

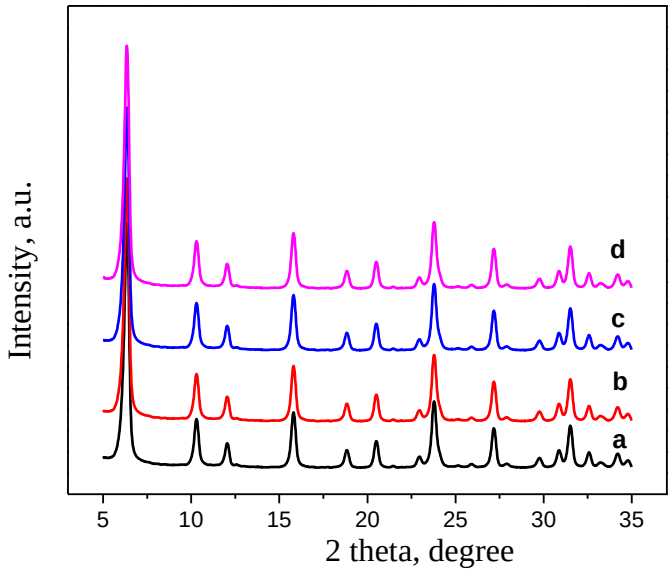

Fig. 1. Wide-angle XRD patterns of gallium-modified HUSY zeolites: (a) HUSY, (b) 1GaHUSY, (c) 2GaHUSY, (d) 3GaHUSY.

10.1002/chem.201701307

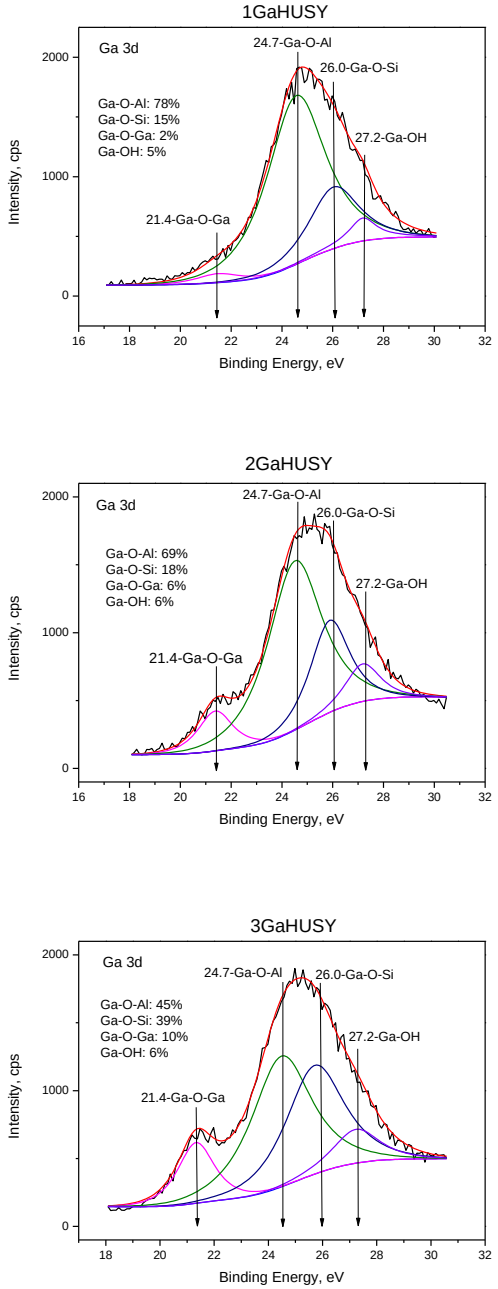

Fig. 2. XPS spectra of Ga 3d for 1GaHUSY, 2GaHUSY and 3GaHUSY.

10.1002/chem.201701307

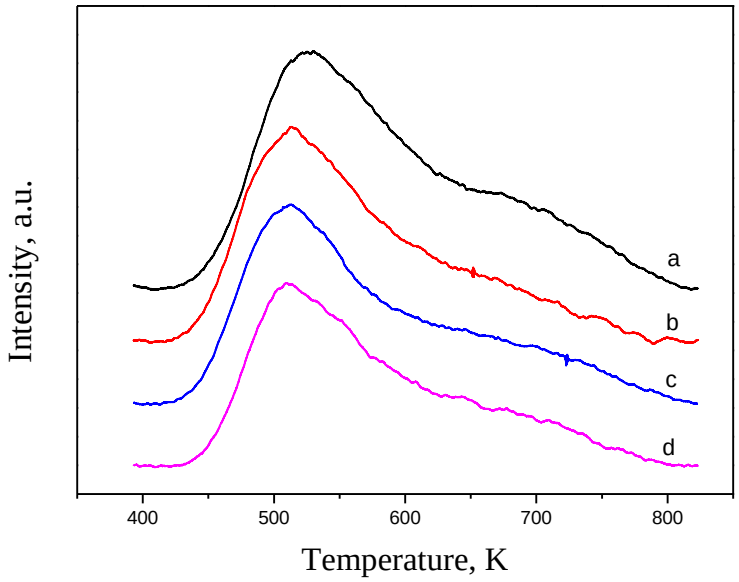

Fig. 3A. NH_3-TPD profiles for (a) HUSY, (b) 1GaHUSY, (c) 2GaHUSY and (d) 3GaHUSY.

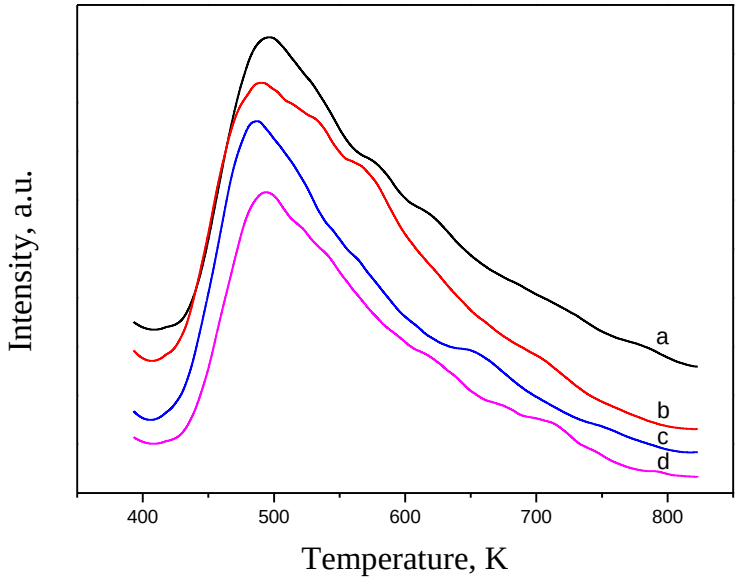

Fig. 3B. NH_3-TPD profiles for (a) NiMo/Y-ASA-A, (b) NiMo/1GaY-ASA-A, (c) NiMo/2GaY-ASA-A and (d) NiMo/3GaY-ASA-A.

10.1002/chem.201701307

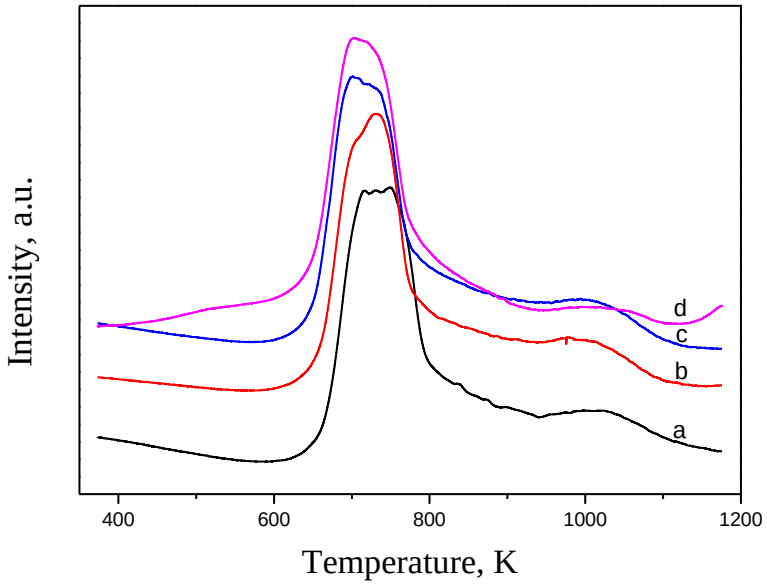

Fig. 4. H_2-TPR profiles for (a) NiMo/Y-ASA-A, (b) NiMo/1GaY-ASA-A, (c) NiMo/2GaY-ASA-A and (d) NiMo/3GaY-ASA-A.

10.1002/chem.201701307

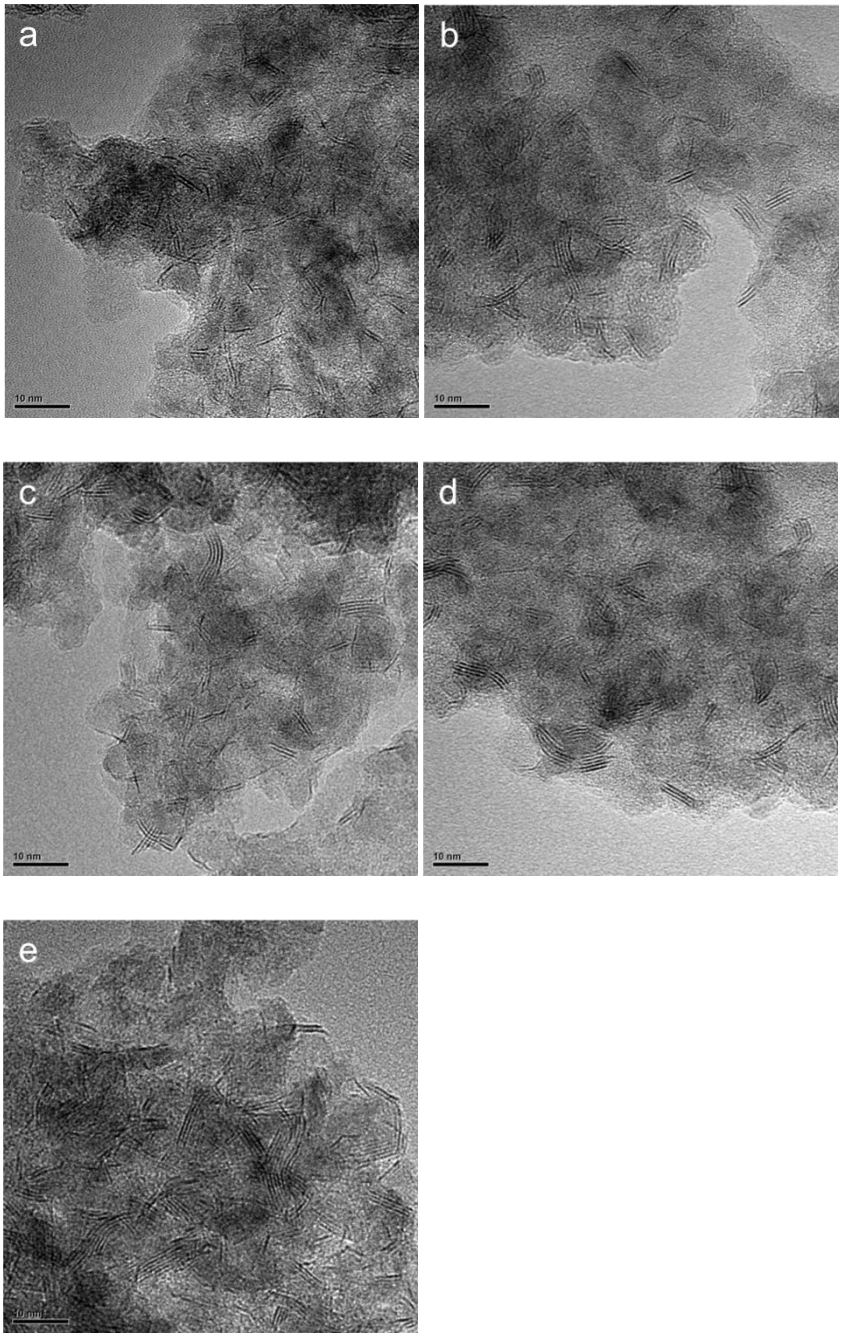

Fig. 5. HRTEM images of the sulfided catalysts: (a) NiMo/ASA-A, (b) NiMo/Y-ASA-A, (c) NiMo/1GaY-ASA-A, (d) NiMo/2GaY-ASA-A, and (e) NiMo/3GaY-ASA-A.

10.1002/chem.201701307

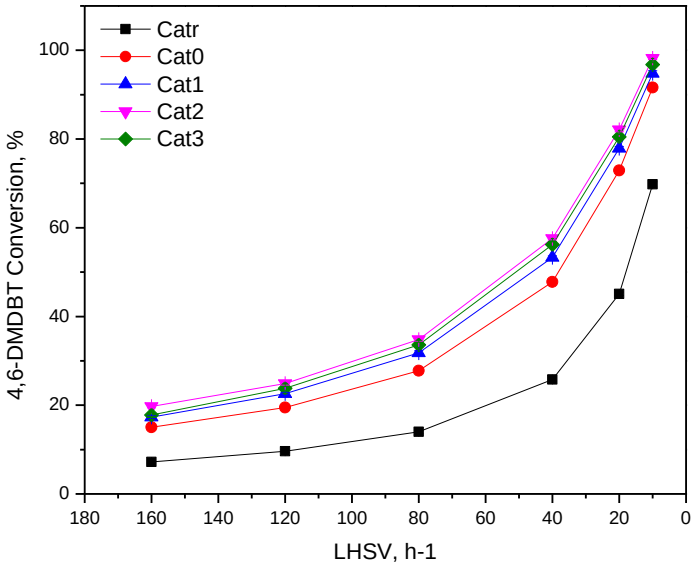

Fig. 6. Conversion of 4,6-DMDBT over different catalysts at different LHSVs.

10.1002/chem.201701307

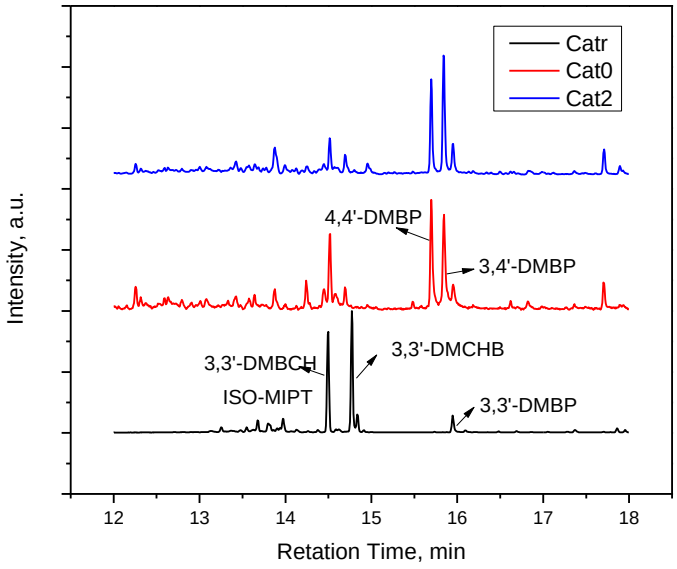

Fig. 7A Comparison of the GC peaks of the products of HDS of 4,6-DMDBT on NiMo/ASA-A, NiMo/Y-ASA-A and NiMo/2GaY-ASA-A at retention times of 12.0 to 18.0 min.

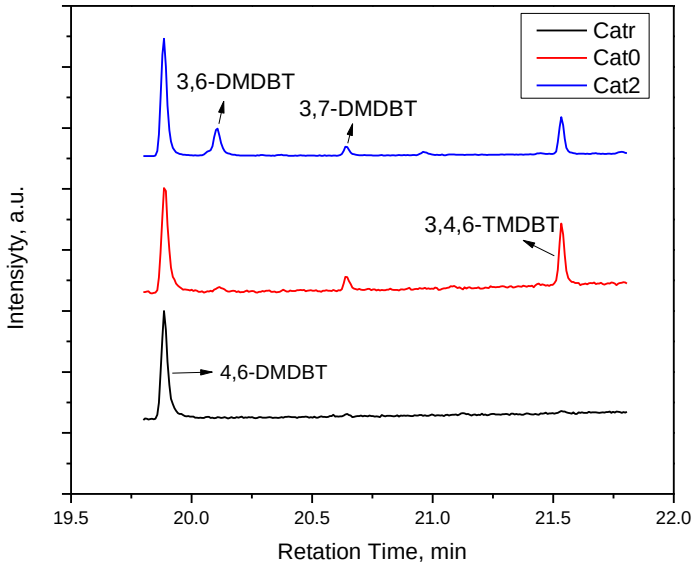

Fig. 7B Comparison of the GC peaks of the products of HDS of 4,6-DMDBT on NiMo/ASA-A, NiMo/Y-ASA-A and NiMo/2GaY-ASA-A at retention times of 19.8 to 21.8 min.

10.1002/chem.201701307

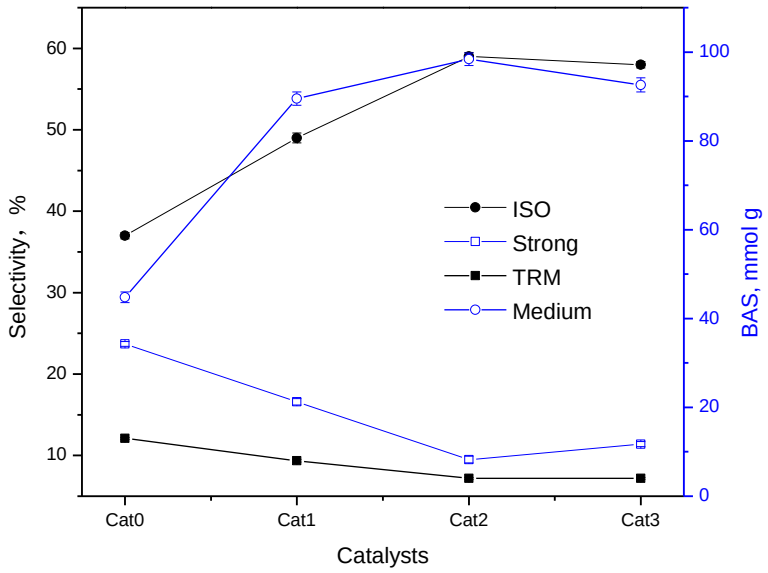

Fig. 8. The relationship between the amount of medium/strong B acid sites and the ISO/TRM selectivity over different catalysts at a reaction temperature of 563 K and LHSV of 40 h^{-1}.

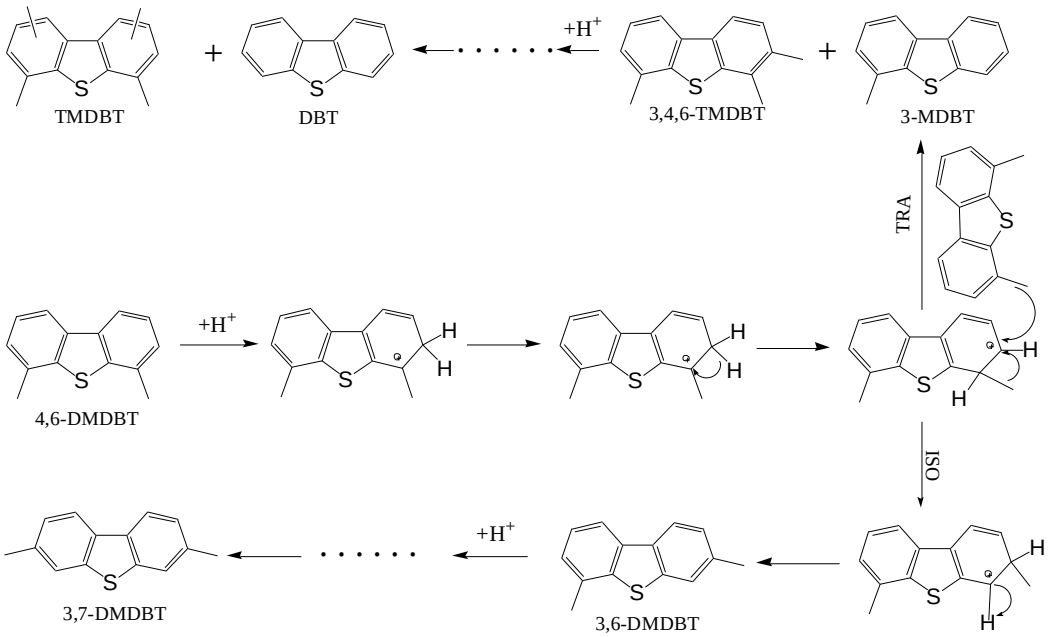

Fig. 9. Isomerization and transmethylation of 4,6-DMDBT over Brønsted acid sites.

10.1002/chem.201701307

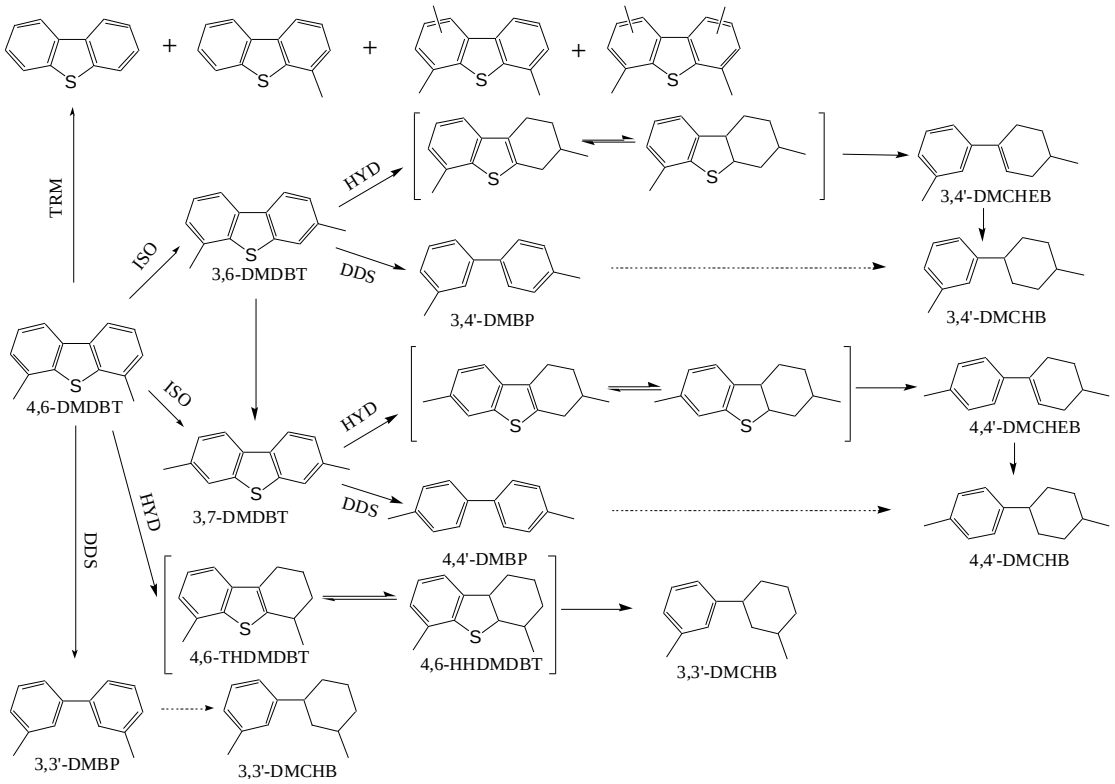

Fig. 10. Reaction network of 4,6-DMDBT HDS over NiMo/2GaY-ASA-A.